

1 **Different effects of anthropogenic emissions and aging processes on the**  
2 **mixing state of soot particles in the nucleation and accumulation**  
3 **modes**

4

5 Yuying Wang<sup>1,2</sup>, Rong Hu<sup>1,2</sup>, Qiuyan Wang<sup>1</sup>, Zhanqing Li<sup>3</sup>, Maureen Cribb<sup>3</sup>, Yele Sun<sup>4</sup>, Xiaorui  
6 Song<sup>1</sup>, Yi Shang<sup>1</sup>, Yixuan Wu<sup>1</sup>, Xin Huang<sup>1</sup>, Yuxiang Wang<sup>1</sup>

7

8 <sup>1</sup> Key Laboratory for Aerosol-Cloud-Precipitation of China Meteorological Administration, School  
9 of Atmospheric Physics, Nanjing University of Information Science & Technology, Nanjing  
10 210044, China

11 <sup>2</sup> State Key Laboratory of Remote Sensing Science, College of Global Change and Earth System  
12 Science, Beijing Normal University, Beijing 100875, China

13 <sup>3</sup> Earth System Science Interdisciplinary Center, Department of Atmospheric and Oceanic Science,  
14 University of Maryland, College Park, MD, USA

15 <sup>4</sup> State Key Laboratory of Atmospheric Boundary Layer Physics and Atmospheric Chemistry,  
16 Institute of Atmospheric Physics, Chinese Academy of Sciences, Beijing, 100029, China

17

18 Correspondence to: Yuying Wang (yuyingwang@nuist.edu.cn)

19 **Abstract.** In this study, the mixing state of size-resolved soot particles and their influencing factors  
20 were investigated based on a five-month aerosol volatility measurement at a suburban site (Xingtai,  
21 XT) in the central North China Plain (NCP). The volatility and mixing state of soot-containing  
22 particles at XT were complex caused by multiple pollution sources and various aging processes.  
23 The results suggest that anthropogenic emissions can weaken the mean volatility of soot-containing  
24 particles and enhance their degree of external mixing. There were fewer externally mixed soot  
25 particles in warm months (June, July, and August) than in cold months (May, September, and  
26 October). Monthly variations in the mean coating depth ( $D_{c,mean}$ ) of volatile matter on soot particles  
27 showed that the coating effect was stronger in warm months than in cold months, even though  
28 aerosol pollution was heavier in cold months. Moreover, the volatility was stronger, and the degree  
29 of internal mixing was higher in nucleation-mode soot-containing particles than in accumulation-  
30 mode soot-containing particles. Relationships between  $D_{c,mean}$  and possible influencing factors  
31 [temperature ( $T$ ), relative humidity (RH), and particulate matter with diameters ranging from 10 to  
32 400 nm] further suggest that high ambient  $T$  and RH in a polluted environment could promote the  
33 coating growth of accumulation-mode soot particles. However, high ambient  $T$  but low RH in a  
34 clean environment were beneficial to the coating growth of nucleation-mode soot particles. Our  
35 results highlight the diverse impact of anthropogenic emissions and aging processes on the mixing  
36 state of soot particles in different modes, which should be considered separately in models to  
37 improve the simulation accuracy of aerosol absorption.

38

## 39 1. Introduction

40 Aerosols are mixed liquid and solid particles suspended in the atmosphere. Some aerosols are  
41 directly produced from natural or anthropogenic sources (i.e., primary aerosols), and the rest are  
42 indirectly transformed from gas precursors through atmospheric chemical reactions (i.e., secondary  
43 aerosols). The newly formed particles can grow or shrink through various aging processes (e.g.,  
44 condensation, coagulation, volatilization, chemical reactions). Aerosol physicochemical properties  
45 (number concentration, shape, mixing state, optical properties, among others) are thus highly  
46 variable. This is one of the reasons why aerosols are highly uncertain in climate change assessments  
47 (Bond et al., 2013; Seinfeld et al., 2016; Bellouin et al., 2020; Christensen et al., 2021). Although  
48 great efforts have been made to understand aerosol optical properties, the uncertainty of radiative  
49 forcing caused by aerosols is still two to three times that of greenhouse gases (IPCC, 2021).

50 Aerosols can affect the earth-atmosphere radiation balance by scattering or absorbing shortwave  
51 and longwave radiation, which is called the aerosol direct climate effect or aerosol-radiation  
52 interactions. Many factors, such as aerosol chemical composition, mixing state, and ambient relative  
53 humidity (RH), have complex impacts on aerosol-radiation interactions (e.g., Twohy et al., 2009;

54 Kuniyal and Guleria, 2019; Ren et al., 2021). According to the sixth IPCC report, the total direct  
55 radiative forcing caused by anthropogenic aerosols is generally negative. However, light-absorbing  
56 carbonaceous particles (LAC) have a warming effect on climate (Ramana et al., 2010; Gustafsson  
57 and Ramanathan, 2016), which can partly offset the cooling effect caused by scattering aerosols,  
58 such as sulfate. Black carbon (BC) is the most important LAC compound, mostly emitted as soot  
59 from anthropogenic sources (incomplete fossil fuel combustion and biomass burning) (Novakov et  
60 al., 2003). Some experiments have suggested that BC in urban polluted environments can play an  
61 important role in pollution formation and development. The internal mixing of BC with secondly  
62 formed matter could also greatly enhance light absorption (Peng et al., 2016; Zhou et al., 2017).

63 The online measurement instruments quantifying the mixing state of BC-containing particles are  
64 limited. Based on the measurement of single-particle soot photometer (SP2), Wu et al. (2017)  
65 indicated that the mass of refractory black carbon (*r*BC) had an approximately lognormal  
66 distribution as a function of the volume-equivalent diameter (VED) in Beijing. Yu et al. (2020)  
67 suggested that the mixing state of *r*BC particles was related to air pollution levels and air mass  
68 sources. Zhang et al. (2021) further indicated that meteorological conditions had a large impact on  
69 the mixing state of *r*BC particles. Moreover, the Aerodyne soot particle aerosol mass spectrometer  
70 (SP-AMS) can also be used to study the mixing state of *r*BC. For example, J. Wang et al. (2019)  
71 found that the formation of secondary aerosols through photochemical and aqueous chemical  
72 reactions was responsible to the coating of *r*BC based on the measurement of SP-AMS in winter  
73 Beijing. However, the lower observation limit of particle size by SP2 and SP-AMS is larger than  
74 ~70 nm. Therefore, they cannot quantify the mixing state of BC-containing particles in the small  
75 nucleation mode.

76 Aerosol volatility refers to the shrinking extent of particles at a certain temperature. The mixing  
77 state of soot particles or tarballs is closely related to aerosol volatility at high temperatures (Philippin  
78 et al., 2004; Wehner et al., 2009; Adachi et al., 2018, 2019). Most primary soot particles from  
79 anthropogenic sources are refractory, hydrophobic, and externally mixed. In a polluted environment,  
80 primary soot particles are easily transformed to internally mixed particles through certain coating  
81 processes in the atmosphere (Cheng et al., 2012; Peng et al., 2016; F. Zhang et al., 2020). However,  
82 coating matter is generally non-refractory because most of the matter consists of secondary chemical  
83 species, such as organics, sulfate, and nitrate (Philippin et al., 2004; Hong et al., 2017). This is why  
84 aerosol volatility can characterize the mixing state of soot particles in polluted environments (Wehner  
85 et al., 2009; Hossain et al., 2012; S. Zhang et al., 2016). A volatility tandem differential mobility  
86 analyzer (VTDMA) is usually used to quantify aerosol volatility by measuring the change in particle  
87 size at a set temperature. Aerosol volatility measured by a VTDMA at a high temperature (> 280°C)  
88 can be used to study the mixing state of soot particles (Philippin et al., 2004; Wehner et al., 2009;

89 Y. Zhang et al., 2016; Wang et al., 2017). Meanwhile, VTDMA measurements are based on the  
90 aerosol number concentration, which is always high in the nucleation mode in the actual atmosphere.  
91 Therefore, VTDMA can quantify the mixing state of nucleation-mode soot particles.

92 Over the past years, several studies have reported the volatility and mixing state of soot-  
93 containing particles based on VTDMA measurements in the North China Plain (NCP). For example,  
94 Wehner et al. (2009) found that the mixing state of soot particles in Beijing and its surrounding  
95 region varied, especially between new particle formation days and heavily polluted days. Using the  
96 same VTDMA and aerosol optical data, Cheng et al. (2009) conducted an aerosol optical closure  
97 study, finding that soot aging was rapid at the Yufa site south of Beijing. The coating on soot particles  
98 can enhance aerosol absorption and scattering coefficients by a factor of 8 to 10 within several hours  
99 due to secondary processing during the daytime, which is the combined effect of the increased  
100 thickness of the coating shell and the transition of soot from an externally mixed state to a coated  
101 state. Cheng et al. (2012) further indicated that aging and emissions were two competing factors in  
102 the mixing state of soot particles. Based on VTDMA measurement data collected in 2015, Wang et  
103 al. (2017) indicated that strict emission control measures implemented in Beijing and surrounding  
104 areas could enhance the volatility of soot-containing particles and their degrees of external mixing.  
105 At another regional site (Xianghe) in the northern part of the NCP, S. Zhang et al. (2016) found that  
106 the mixing state of ambient particles was complex with different volatilities. Furthermore, Y. Zhang  
107 et al. (2016) suggested that the average shell-to-core ratio and absorption enhancement ( $E_{ab}$ ) of  
108 ambient BC was 2.1–2.7 and 1.6–1.9, respectively.

109 These studies imply that anthropogenic emissions play an important role in the volatility and  
110 mixing state of soot-containing particles and that the coating on soot particles can greatly enhance  
111 aerosol absorption. However, these studies were based on data collected during short-term  
112 observational periods in the northern part of the NCP and they did not distinguish the factors  
113 influencing the mixing state of nucleation- and accumulation-mode soot particles. Recent studies  
114 (Y. Wang et al., 2018, 2019, 2021) have shown that anthropogenic sources and aerosol aging  
115 processes are various in the north and central-south NCP, leading to diverse aerosol physiochemical  
116 properties between these regions in different seasons. More research about the mixing state of soot  
117 particles in the central-south NCP is needed to improve the accuracy of modeled aerosol optical  
118 properties.

119 This study investigates for the first time the volatility and mixing state of nucleation- and  
120 accumulation-mode soot-containing particles in the warm and cold seasons based on one  
121 comprehensive field campaign that took place in the central NCP, lasting five months. Exploring  
122 factors influencing the volatility and mixing state of soot-containing particles in this study will  
123 improve the accuracy of modeled aerosol optical properties in the central NCP. This paper is

124 organized as follows. Section 2 introduces the sampling site, instruments, and data analysis. Section  
125 3 presents the results and discussion, including meteorological conditions, aerosol pollution levels,  
126 changes in volatility and mixing state of soot-containing particles, and their influencing factors.  
127 Section 4 gives conclusions and summarizes the study.

128

## 129 2. Sampling site, instruments, and data analysis

### 130 2.1 Sampling site

131 Data used in this study were collected at the National Meteorological Basic Station ( $37^{\circ}11'N$ ,  
132  $114^{\circ}22'E$ , 180 m above sea level) in Xingtai (XT), China, equipped with a variety of meteorological  
133 observation instruments. The measured meteorological variables including ambient temperature,  
134 relative humidity (RH), wind direction and speed was used in this study. Y. Wang et al. (2018)  
135 reported that this site is located in a polluted area of the central-south NCP, influenced by multiple  
136 anthropogenic sources, such as industrial coal firing, fossil-fuel burning, agricultural activities, and  
137 household emissions. The long-distance transport of pollutants also influences the air quality at XT.  
138 Previous studies have suggested that air pollution at XT represents well regional pollution  
139 characteristics in the central NCP east of the Taihang Mountains (Y. Zhang et al., 2018; Y. Wang et  
140 al., 2018). A comprehensive field campaign named the Atmosphere-Aerosol-Boundary layer-Cloud  
141 ( $A^2BC$ ) Interaction Joint Experiment was carried out at XT from May to October of 2016. Y. Wang  
142 et al. (2018) and Li et al. (2019) provide details about the XT site and the  $A^2BC$  campaign. Here,  
143 over five months of aerosol observational data, including particle number size distribution (PNSD),  
144 aerosol volatility, and BC mass concentration, were used to analyze the volatility and mixing state  
145 of soot particles and their influencing factors.

146

### 147 2.2 Instruments

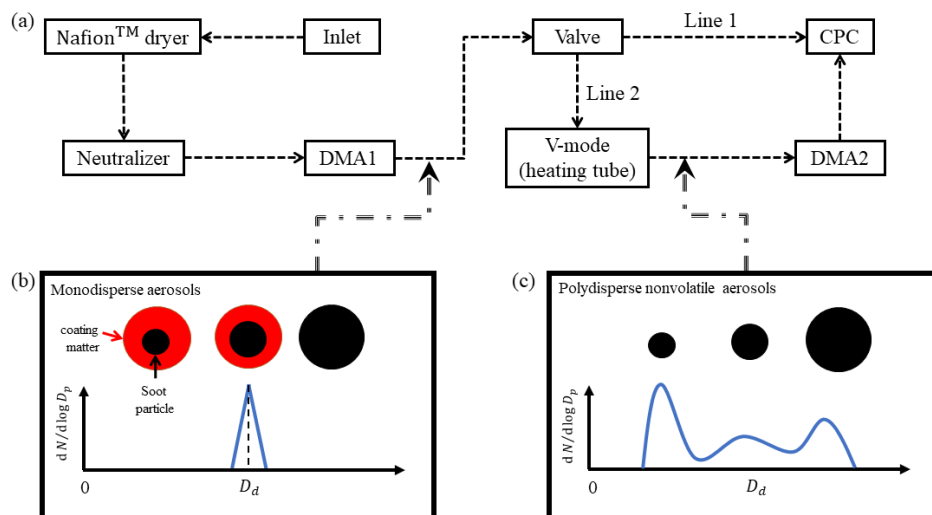
#### 148 2.2.1 Measuring PNSD and aerosol volatility

149 The tandem differential mobility analyzer (TDMA) system is widely used to measure the change  
150 in particle size under special conditions, e.g., high humidity, high temperature, and chamber  
151 chemical reactions (Swietlicki et al., 2008). In this campaign, the VTDMA system was used to  
152 measure aerosol volatility at  $300^{\circ}C$ . The inlet air sample was first dried by a Nafion<sup>TM</sup> dryer to low  
153 RH ( $< 30\%$ ), then neutralized by a soft X-ray neutralizer (model 3088, TSI Inc.; Fig. 1a). Afterwards,  
154 quasi-monodisperse aerosols (Fig. 1b) with a certain dried diameter ( $D_d$ ) were split by the first  
155 differential mobility analyzer (DMA1). In this campaign,  $D_d$  was set to 40, 80, 110, 150, 200, and  
156 300 nm. An automated valve located after the DMA1 had two outlet lines. Line 1 directly accessed  
157 the water-based condensation particle counter (WCPC, model 3787, TSI Inc.), measuring the  
158 number concentration of particles ranging from 10 to 400 nm. Line 2 accessed a heating tube,

159 vaporizing volatile materials at a controlled high temperature (300°C in this study). The ratio of  
 160 particle size after volatilization [ $D_p(T)$ ] to  $D_d$  is defined as the aerosol shrink factor (i.e.,  $SF = D_p(T)$   
 161 /  $D_d$ ). After heating, residual aerosols were generally polydisperse nonvolatile particles (Fig. 1c).  
 162 The second DMA (DMA2) and WCPC were used to measure the number size distribution of  
 163 nonvolatile particles, measuring the distribution function of  $SF$  ( $SF$ -MDF). Finally, the probability  
 164 density function of  $SF$  ( $SF$ -PDF) was retrieved using the TDMAfit algorithm (Stolzenburg and  
 165 McMurry, 1988; Stolzenburg and McMurry, 2008).

166 In this study, we assume that the shape of all particles follows the core-shell model (nonvolatile  
 167 core and volatile shell; Fig. 1b). Residual particles after volatilization have different-sized  
 168 nonvolatile cores (Fig. 1c). Previous studies have suggested that residual particles at 300°C mainly  
 169 consist of soot (Philippin et al., 2004; Wehner et al., 2009). Aerosol volatility measured by the  
 170 VTDMA in this study can thus reflect the degree of mixing state of soot particles.

171



172

173 **Figure 1.** Schematic diagram of the volatility tandem differential mobility analyzer used in this  
 174 study.

175

### 176 2.2.2 Measuring BC

177 In this campaign, a seven-wavelength aethalometer (model AE-33, Magee Scientific Corp.) was  
 178 used to measure the mass concentration of BC ( $M_{BC}$ ). After calibration, the sampling flow rate of  
 179 the AE-33 was 5.0 L min<sup>-1</sup>. A cyclone with particulate matter (diameters = 2.5 μm, or PM<sub>2.5</sub>) was  
 180 used in the sample inlet. Aerosol particles were collected on filter tape through a spot, and the  
 181 instantaneous concentration of optically absorbing aerosols was retrieved from the rate of change  
 182 of the attenuation of light transmitted through the filter. The wavelength channels of the AE-33 were  
 183 370, 470, 525, 590, 660, 880, and 940 nm. According to the manufacturer's instructions, the  $M_{BC}$  is  
 184 calculated from the change in optical attenuation at channel 6 (i.e., 880 nm) in the selected time

185 interval using the mass absorption cross section (MAC) of  $7.77 \text{ m}^2 \text{ g}^{-1}$ . The dependency of MAC on  
186 BC coating may introduce some uncertain in calculating MAC (Drinovec et al., 2015)..

187

### 188 2.2.3 VTDMA data analysis

189 The retrieved  $SF$ -PDF ( $c(D_d, SF)$ ) is normalized as  $\int c(D_d, SF) dSF = 1$ . The ensemble mean  
190 shrink factor ( $SF_{\text{mean}}$ ) is then calculated as

$$191 SF_{\text{mean}}(D_d) = \int_0^{\infty} SF \cdot c(D_d, SF) dSF . \quad (1)$$

192 Particles can be classified into several volatile groups according to different  $SF$  ranges (Y.  
193 Wang et al., 2017). The number fraction ( $NF$ ) for each volatile group with the  $SF$  boundary of [a, b]  
194 is calculated as

$$195 NF(D_d) = \int_a^b c(D_d, SF) dSF . \quad (2)$$

196 Based on the core-shell assumption, the coating depth ( $D_c$ ) of soot particles is defined as the  
197 depth of shell materials (i.e., shell depth). According to the definition of  $SF$ ,  $D_c$  for the particle  
198 ( $D_d, SF$ ) can be calculated as

$$199 D_c(D_d, SF) = \frac{D_d}{2} (1 - SF). \quad (3)$$

200 The ensemble mean  $D_c$  ( $D_{c,\text{mean}}$ ) using the normalized  $SF$ -PDF data is then calculated as

$$201 D_{c,\text{mean}}(D_d) = \int_0^{\infty} D_c(D_d, SF) \cdot c(D_d, SF) dSF . \quad (4)$$

202

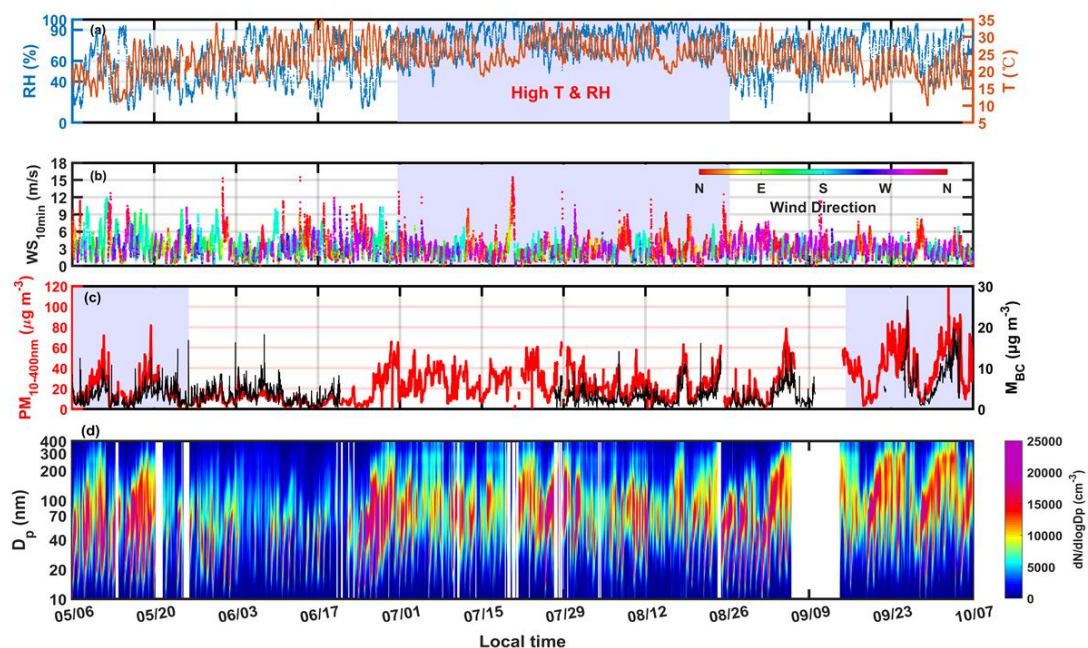
## 203 3. Results and discussion

### 204 3.1 Meteorological conditions and aerosol pollution levels

205 Figure 1a-b shows the time series of ambient temperature ( $T$ ), RH, and wind direction and  
206 speed (WD and WS, respectively) during the campaign. Monthly changes in  $T$  are clearly seen (Fig.  
207 2a). Average  $T$ s in warm (June, July, and August) and cold (May, September, and October) months  
208 were  $25.73 \pm 3.80$  and  $19.0 \pm 5.74^\circ\text{C}$ , respectively. Figure 2a also suggests that RH was higher in July  
209 and August than in other months.

210 Figure 2b shows that the wind changed significantly in different months at XT. Monthly wind  
211 rose diagrams (Fig. S1) indicate that northwest winds prevailed in all months, caused by the special  
212 terrain around XT (Y. Zhang et al., 2018). In July, weak southeast winds were also present,  
213 beneficial to the accumulation of air pollutants due to the stable atmospheric environment. In August,  
214 the other prevailing wind was from the north, which was beneficial for atmospheric diffusion.

215



216

217 **Figure 2.** Time series of (a) ambient relative humidity (RH; unit: %)

218 and temperature ( $T$ ; unit: °C),

219 (b) wind direction (WD) and 10-minute-averaged wind speed (WS; unit: m s<sup>-1</sup>),

220 (c) mass concentration of 10–400 nm particles (PM<sub>10-400</sub>, in red; unit: μg m<sup>-3</sup>), assuming that the aerosol

221 density is 1.6 g cm<sup>-3</sup>, and mass concentration of black carbon ( $M_{BC}$ , in black; unit: μg m<sup>-3</sup>), and (d)

222 particle number size distribution at the Xingtai site from 6 May 2016 to 6 October 2016.

223 In this study, the total mass concentration of 10–400-nm particles (PM<sub>10-400</sub>) (Fig. 2c) was

224 calculated using PNSD data (Fig. 2d), assuming that the aerosol density was 1.6 g cm<sup>-3</sup> (Y. Wang

225 et al., 2017). The average PM<sub>10-400</sub> concentrations in warm and cold months were 19.68±13.58 and

226 29.79±21.37 μg m<sup>-3</sup>, respectively, indicating much higher aerosol pollution in cold months than in

227 warm months. In cold months, PM<sub>10-400</sub> accumulated periodically as accumulation-mode ( $D_p > 100$

228 nm) particles increased. This is closely related to cyclic changes in general atmospheric circulation,

229 reflected by the cycle of winds (Fig. 2b). However, PM<sub>10-400</sub> was lower in May than in September

230 and October, likely due to the weaker particle growth in May. During warm months, PM<sub>10-400</sub>

231 reached its lowest value in June with the lowest number concentration of accumulation-mode

232 particles of all months (Fig. S2), suggesting that meteorological conditions in June were not

233 conducive to particle growth. The high  $T$  and RH in July and August were beneficial to particle

234 growth by promoting atmospheric photochemical and liquid chemical reactions (Z. Wu et al., 2018;

235 Peng et al., 2021). Figure 2c suggests that PM<sub>10-400</sub> was much higher in July and August than in June,

236 although the mass concentrations of black carbon ( $M_{BC}$ s) in these months were considerable.

237 However, PM<sub>10-400</sub> was lower in August than in July, likely because of the better atmospheric

238 diffusion conditions (more and stronger northerly winds) in August. Figure 2c also shows that

239 changes in  $M_{BC}$  and PM<sub>10-400</sub> were similar, suggesting the possible role of BC in the formation



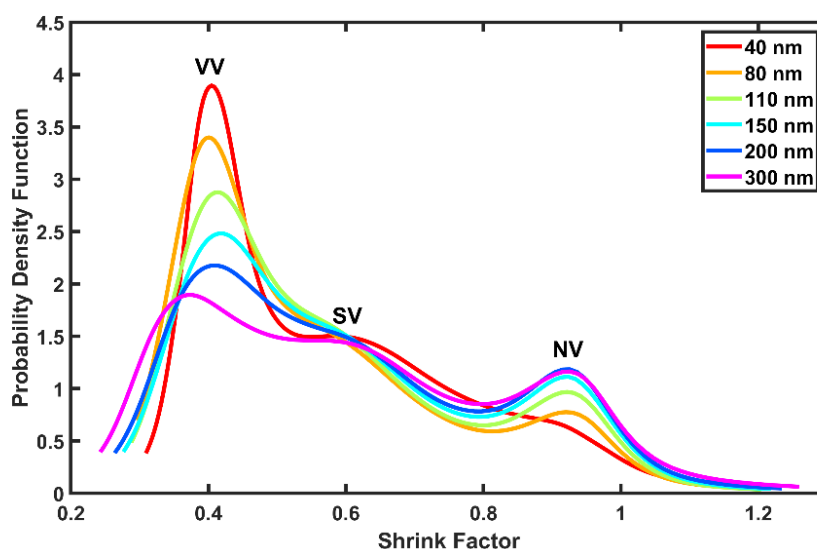
240 processes of aerosol pollution. Recently, F. Zhang et al. (2020) demonstrated that BC-catalyzed  
241 sulfate formation involving  $\text{NO}_2$  and  $\text{NH}_3$  plays an important role in the formation of haze events.

242

### 243 3.2 Monthly and diurnal variations in $SF$ -PDF

244 Figure 3 shows the size-resolved mean  $SF$ -PDFs at XT. In general,  $SF$ -PDFs had three peak  
245 modes, namely, at  $SF \approx 0.4$  [very volatile (VV) mode], 0.6 [slightly volatile (SV) mode], and 0.9  
246 [nonvolatile (NV) mode]. The trimodal distributions of  $SF$ -PDFs at XT in the central NCP differ  
247 from those at sites in the northern NCP (S. Zhang et al., 2016; Y. Wang et al., 2017), implying  
248 highly complex volatility and mixing state of soot particles at XT. Note that the  $SF$ -PDF of 40-nm  
249 particles has a quasi-unimodal distribution pattern, with low fractions of NV- and SV-mode  
250 particles. Previous studies have indicated that most NV-mode particles are externally mixed soot  
251 particles (Cheng et al., 2012; Cheung et al., 2016). This suggests that soot-containing particles in  
252 nucleation mode (represented by 40-nm particles) in this study had strong volatility and a high  
253 degree of internal mixing. Figure 3 also suggests that the fraction of NV-mode particles increased  
254 with increasing particle size, indicating a higher fraction of externally mixed soot particles in  
255 accumulation mode. This is related to the primary size of soot particles. Some studies suggest that  
256 freshly emitted refractory particles (like BC) are primarily in accumulation mode. For example,  
257 Levy et al. (2013) reported that fresh BC was mostly in the 150–240 nm size range, while Wu et  
258 al. (2017) reported that refractory BC size distribution measurements in Beijing peaked at about  
259 200 nm, with a secondary less significant mode at about 600 nm.

260

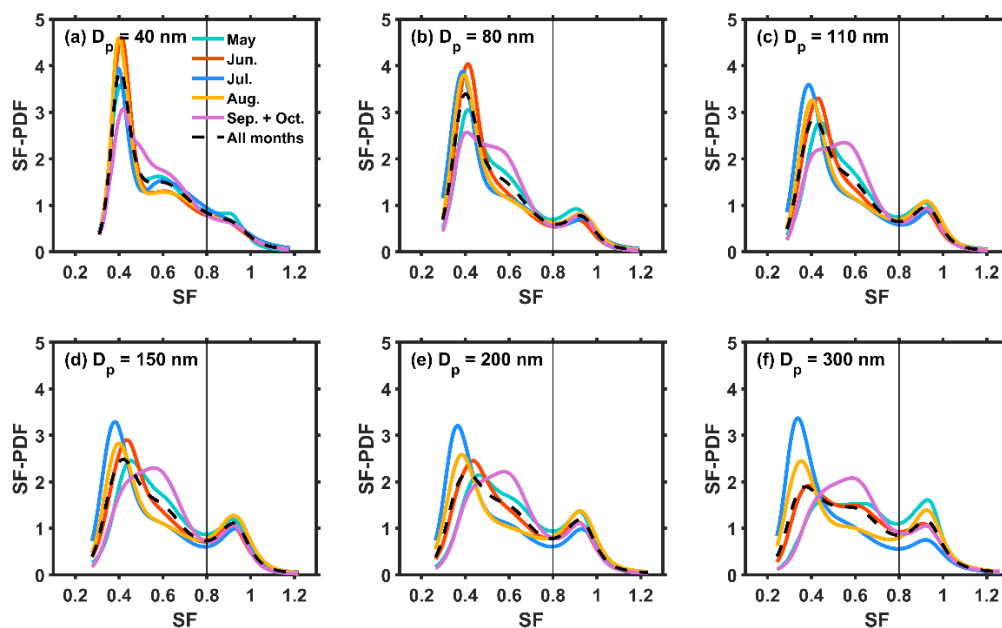


261

262 **Figure 3.** Size-resolved mean probability density functions of the shrink factor at different  
263 wavelengths. VV stands for “very volatile”, SV stands for “slightly volatile”, and NV stands for  
264 “non-volatile”.

265

266 Figure 4a-b shows that VV-mode fractions in the  $SF$ -PDFs of 40-nm and 80-nm particles were  
 267 higher in warm months than in cold months, indicating that nucleation-mode soot particles were  
 268 more volatile in warm months. Our previous study has shown that new particle formation (NPF)  
 269 events occurred frequently at XT (Y. Wang et al., 2018). Wehner et al. (2009) reported that most  
 270 newly formed matter is composed of organics and sulfate, easily volatilized at 300°C. All this implies  
 271 that coating by newly formed secondary matter was the possible reason for the high volatility of  
 272 nucleation-mode soot-containing particles in warm months. For accumulation-mode (110–300 nm)  
 273 particles (Fig. 4c-f), monthly changes in  $SF$ -PDF patterns are clearly seen. In general,  $SF$  peak  
 274 values of the VV mode were smaller (meaning a thicker coating of volatile matter), and fractions of  
 275 VV-mode particles were higher in warm months (especially in July) than in cold months, indicating  
 276 that the coating on accumulation-mode soot particles was also stronger in warm months than in cold  
 277 months. As previously mentioned, meteorological conditions in warm months (i.e., high  $T$  and RH)  
 278 were favorable to the particle growth of soot particles through atmospheric photochemical and liquid  
 279 chemical reactions. In cold months (May, September, and October), the volatility of accumulation-  
 280 mode soot-containing particles was relatively lower, indicating thinner coating matter on the  
 281 surfaces of soot particles in the polluted cold environment. This is consistent with measurements  
 282 made at an urban site in Beijing (Yu et al., 2020). Yu et al. (2020) also suggests that a more even  
 283 distribution of  $rBC$  and non- $rBC$  material mass fractions in summer than in winter, which may be  
 284 caused by higher amount of secondary material.  
 285



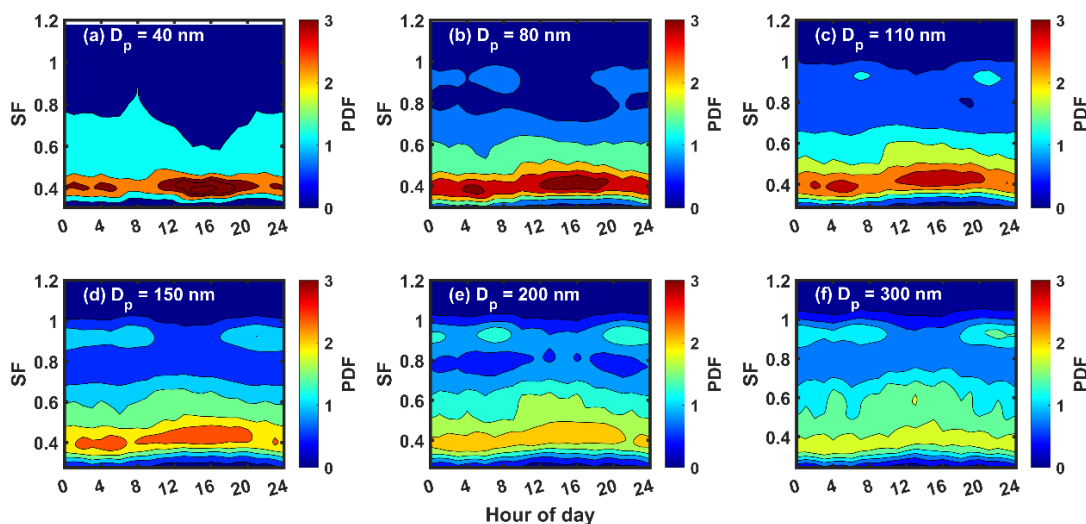
286

287 **Figure 4.** Monthly variations in the mean shrink factor ( $SF$ ) probability distribution functions ( $SF$ -  
 288 PDFs) for particles with diameters of (a) 40 nm, (b) 80 nm, (c) 110 nm, (d) 150 nm, (e) 200 nm,  
 289 and (f) 300 nm.

290

291 Figure 5 shows diurnal variations in  $SF$ -PDF for different size particles, illustrating the distinct  
292 diurnal variation patterns of  $SF$ -PDF for nucleation- and accumulation-mode particles. VV-mode  
293 fractions for 40-nm and 80-nm particles ( $\sim SF = 0.4$ ) increased sharply from around noon into the  
294 afternoon (Fig. 5a-b). Figure S3 shows that the number concentration of 40-nm and 80-nm particles  
295 increased quickly due to the influence of NPF events. This further corroborates that newly formed  
296 particles created during NPF events are the possible coating matter on nucleation-mode soot  
297 particles. Figure 5c-f suggests that NV-mode fractions in accumulation-mode soot particles ( $\sim SF =$   
298  $0.9$ ) were higher than those in nucleation-mode soot particles and that these fractions became higher  
299 with increasing particle size. NV-mode fractions in accumulation-mode soot particles clearly  
300 increased during the morning and evening rush hours. This suggests that anthropogenic emissions  
301 have a large impact on the volatility and mixing state of soot particles, especially for accumulation-  
302 mode soot particles. Previous studies have shown that some of the primary pollutants generated by  
303 human activities are composed of refractory materials, such as BC (Philippin et al., 2004; Levy et  
304 al., 2014). An increase in primary refractory particles could weaken the ensemble volatility and  
305 mixing state of soot particles. Figure 3c-f also shows that the NV-mode fraction in the  $SF$ -PDF of  
306 accumulation-mode particles decreased sharply in the daytime, likely caused by the coating effect  
307 of volatile matter through photochemical reactions.

308



309

310 **Figure 5.** Diurnal variations in size-resolved shrink factor ( $SF$ ) probability distribution functions  
311 (PDFs) for particles with diameters of (a) 40 nm, (b) 80 nm, (c) 110 nm, (d) 150 nm, (e) 200 nm,  
312 and (f) 300 nm.

313

314 In summary, the volatility and mixing state of soot-containing particles were complex at XT

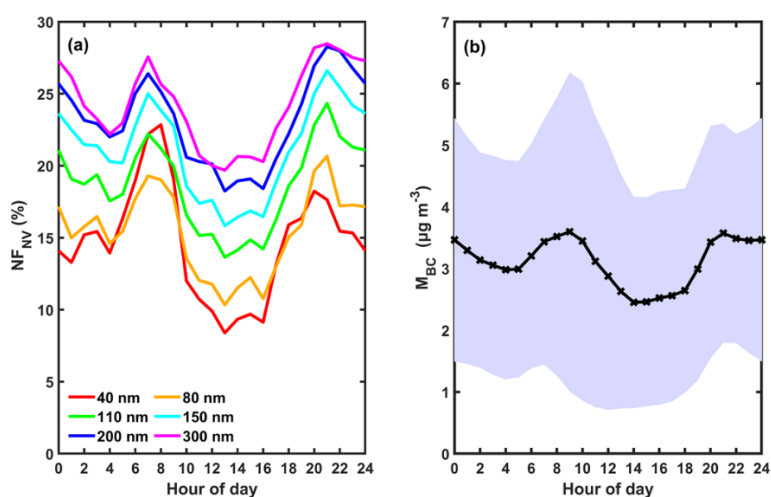
315 during the field campaign. Soot-containing particles in the nucleation mode had strong volatility  
 316 and a high degree of internal mixing, likely due to the impact of frequent NPF events that occurred  
 317 during this campaign. The strong volatility and high degree of internal mixing in warm months were  
 318 likely caused by the aging processes of particles. Anthropogenic emissions also had a large impact  
 319 on the volatility and mixing state of soot particles, especially in the accumulation mode. The impacts  
 320 of anthropogenic emissions and secondary chemical reactions on the volatility and mixing state of  
 321 soot particles will be further discussed next.

322

### 323 3.3 Factors influencing the volatility and mixing state of soot particles

#### 324 3.3.1 The impact of anthropogenic emissions on the volatility and mixing state of soot 325 particles

326 As previously discussed, soot particles from anthropogenic emissions were always refractory and  
 327 nonvolatile at 300°C. Analyzing the relationship between the number fraction of nonvolatile-mode  
 328 particles ( $NF_{NV}$ ,  $SF > 0.8$ ) in  $SF$ -PDFs and  $M_{BC}$  can verify this because BC is the main matter in  
 329 soot particles. Figure 6a shows that  $NF_{NV}$  reached two peak values, one during the morning rush  
 330 hour at about 08:00 and the other during the evening rush hour at about 20:00.  $M_{BC}$  also reached  
 331 two peak values at those same times (Fig. 6b). Overall, the diurnal variation trends of  $NF_{NV}$  for all  
 332 sizes and  $M_{BC}$  were similar. This suggests the great impact of anthropogenic BC on the volatility  
 333 and mixing state of soot particles.  $NF_{NV}$  decreased quickly after rush hours, especially in the  
 334 morning (Fig. 6a), suggesting that the aging processes of primary soot particles were quick at this  
 335 heavily polluted site. Cheng et al. (2012) also observed the same phenomenon at a suburban site in  
 336 Beijing.



337

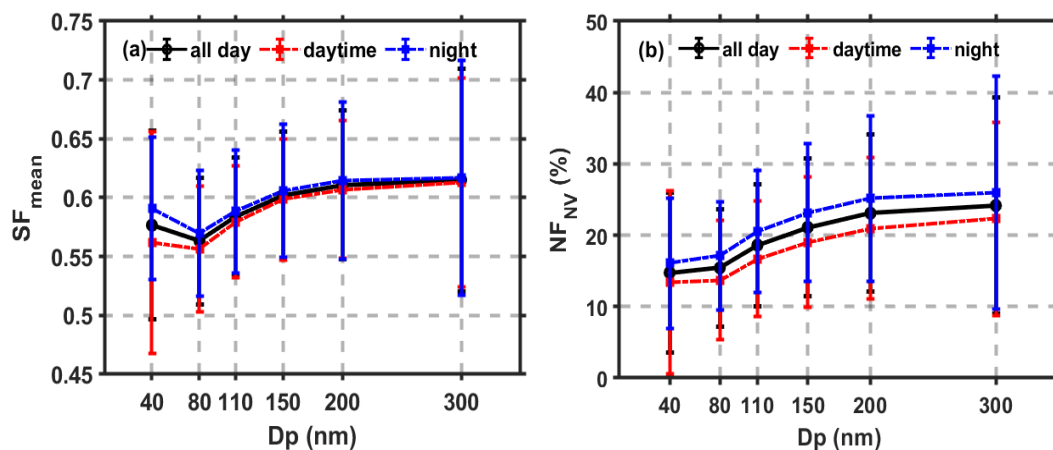
338 **Figure 6.** Diurnal variations in (a) wavelength-dependent, size-resolved number fractions of  
 339 nonvolatile particles ( $NF_{NV}$ ), and (b) mass concentration of black carbon ( $M_{BC}$ ). The purple,  
 340 shaded area shows the standard deviations of  $M_{BC}$ .

341

342 3.3.2 The impact of aging processes on the volatility and mixing state of soot-containing  
343 particles

344 Lower  $SF_{\text{mean}}$  values mean stronger aerosol volatility, indicating a larger coating depth of volatile  
345 matter on soot particles. Figure 7a suggests that volatility is stronger during daytime than at night  
346 (i.e., a lower  $SF_{\text{mean}}$ ), particularly for 40-nm particles. This illustrates the large impact of  
347 photochemical reactions on the volatility and mixing state of soot particles. Figure 7a also suggests  
348 that the  $SF_{\text{mean}}$  of 80-nm particles was lower than that of 40-nm particles. Wang et al. (2018) suggests  
349 that aerosol hygroscopicity of 40-nm particles is larger than that of 80-nm particles during the  
350 daytime at this site. These indicate the great impact of photochemical reactions on the  
351 physicochemical properties of nucleation-mode particles. Inversely,  $SF_{\text{mean}}$  increased with  
352 increasing particle size in the accumulation mode (110–300 nm), suggesting weaker volatility and  
353 a smaller coating depth for larger accumulation-mode soot particles.

354



355

356 **Figure 7.** (a) Size-resolved ensemble mean shrink factors ( $SF_{\text{mean}}$ ) and (b) size-resolved number  
357 fractions of nonvolatile particles ( $NF_{\text{NV}}$ ) during the 24-hr day (black solid lines), during daytime  
358 (red dotted lines), and during nighttime (blue dotted lines). The error bars denote standard deviations.

359 Figure 8 shows the diurnal variation in  $SF_{\text{mean}}$  in different months for different particle sizes.  
360 Figure 8a-b shows that the  $SF_{\text{mean}}$  of 40-nm and 80-nm particles clearly increased during the  
361 morning and evening rush hours in all months. However, the  $SF_{\text{mean}}$  of 40-nm and 80-nm particles  
362 decreased sharply in the afternoon. This suggests that the volatility of nucleation-mode soot-  
363 containing particles was easily influenced by anthropogenic emissions during rush hours and  
364 photochemical reactions in the daytime. The diurnal variation patterns of  $SF_{\text{mean}}$  (Fig. 8c-f) in the  
365 accumulation mode were diverse in different months. The  $SF_{\text{mean}}$  in warm months was usually lower  
366 than in cold months, indicating a larger impact of aging processes on the volatility of accumulation-  
367 mode soot-containing particles in warm months. Figure 8c-f also shows that the  $SF_{\text{mean}}$  in

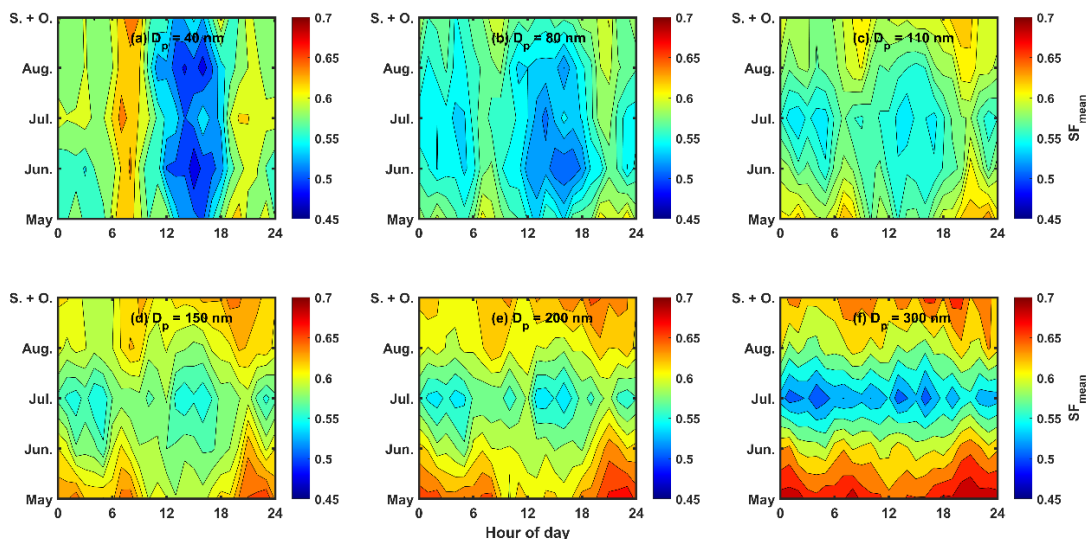
368 accumulation mode was lowest in July. This suggests that high  $T$ , high RH, and the stable  
369 atmospheric environment in July were conducive to the coating of secondary matter on  
370 accumulation-mode soot particles, a possible reason for the high aerosol pollution levels in July.  
371 Moreover, Fig. 8 suggests that monthly variations in  $SF_{\text{mean}}$  became larger with increasing particle  
372 size. The seasonal variation in the coating effect should thus be considered when modeling  
373 physicochemical properties of soot particles, especially larger particles.

374 To further investigate the impact of aging processes on the mixing state of soot particles, size-  
375 resolved  $NF_{\text{NV}}$  in the daytime and at night were compared (Fig. 7b).  $NF_{\text{NV}}$  was always lower in the  
376 daytime than at night, meaning that the fraction of externally mixed soot particles in the daytime  
377 was lower. This further indicates that photochemical reactions in the daytime can transform  
378 externally mixed soot particles into internally mixed soot particles. Figure 7b also shows that  $NF_{\text{NV}}$   
379 increased with increasing particle size, meaning a higher degree of external mixing of larger  
380 particles. This suggests that the degree of external mixing was higher for accumulation-mode soot  
381 particles than nucleation-mode particles.

382 The diurnal variation patterns of  $NF_{\text{NV}}$  (Fig. S4) and  $SF_{\text{mean}}$  (Fig. 8) in different months were  
383 similar. Externally mixed soot particles increased during the morning and evening rush hours due  
384 to enhanced anthropogenic emissions. Monthly differences in  $NF_{\text{NV}}$  increased with increasing  
385 particle size. Figure S4 also shows a lower number fraction of externally mixed soot particles (i.e.,  
386 a smaller  $NF_{\text{NV}}$ ) in warm months than in cold months.

387 These results illustrate the distinct volatilities and mixing states of soot particles between the  
388 nucleation and accumulation modes. A lower degree of external mixing and thicker coating depth  
389 in nucleation-mode particles exists. It is thus important to quantify the impact of the coating effect  
390 for nucleation-mode soot particles when studying aerosol physicochemical properties. The next  
391 section analyzes the coating depth and its influencing factors.

392



393

394 **Figure 8.** Diurnal variations in ensemble mean shrink factor ( $SF_{\text{mean}}$ ) in different months for  
 395 different particle sizes.

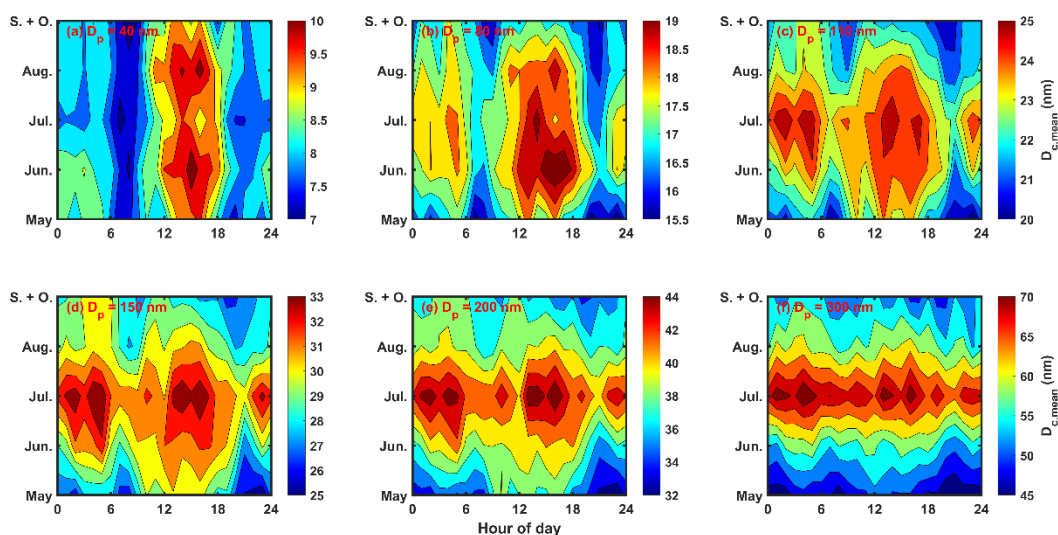
396

### 397 3.4 The coating depth of secondary matter on soot particles

398 The ensemble mean coating depth on soot particles ( $D_{c,\text{mean}}$ ) can be calculated using Eq. (4).

399 Figure 9 shows diurnal variations in  $D_{c,\text{mean}}$  in different months for different particle sizes. The  
 400 diurnal variation patterns of  $D_{c,\text{mean}}$  for nucleation-mode and accumulation-mode soot particles  
 401 differ greatly. The diurnal variation patterns of  $D_{c,\text{mean}}$  in different months were similar for  
 402 nucleation-mode soot particles (40-nm and 80-nm particles) but not for accumulation-mode soot  
 403 particles (110–300-nm particles). The enhancement of  $D_{c,\text{mean}}$  in the daytime occurred in all months  
 404 for nucleation-mode soot particles but only in the warm months for accumulation-mode soot  
 405 particles. At night, the enhancement of  $D_{c,\text{mean}}$  for accumulation-mode soot particles was strong,  
 406 especially in warm months. However, it was weak for nucleation-mode soot particles. These all  
 407 imply large differences in  $D_{c,\text{mean}}$  in different months for nucleation-mode and accumulation-mode  
 408 soot particles, likely caused by variations in meteorological conditions and aerosol pollution levels.

409



410

411 **Figure 9.** Diurnal variations in ensemble mean coating depth ( $D_{c,\text{mean}}$ ) on soot particles in different  
 412 months for different particle sizes. Note that the color bars have different ranges of values in each  
 413 panel.

414

415 The relationships between  $D_{c,\text{mean}}$  and several possible influencing factors ( $T$ , RH, and  $\text{PM}_{10-400\text{nm}}$ )  
 416 were further analyzed (Fig. 10). Figures 10a and 10d show positive correlations between  
 417  $D_{c,\text{mean}}$  and  $T$  for both nucleation-mode and accumulation-mode particles (represented by 40-nm and  
 418 300-nm particles, respectively). This is consistent with the results shown in Fig. 7. Zhang et al.  
 419 (2021) also indicated that warm environments were favorable to the aging of  $r\text{BC}$ . The high daytime  
 420  $T$  was conducive to the aging of soot particles caused by strong photochemical reactions. However,  
 421 the relationships between RH and  $D_{c,\text{mean}}$  (Figs. 9b and 9e) and between  $\text{PM}_{10-400\text{nm}}$  and  $D_{c,\text{mean}}$  (Figs.  
 422 9c and 9f) were inverse between nucleation- and accumulation-mode soot particles.

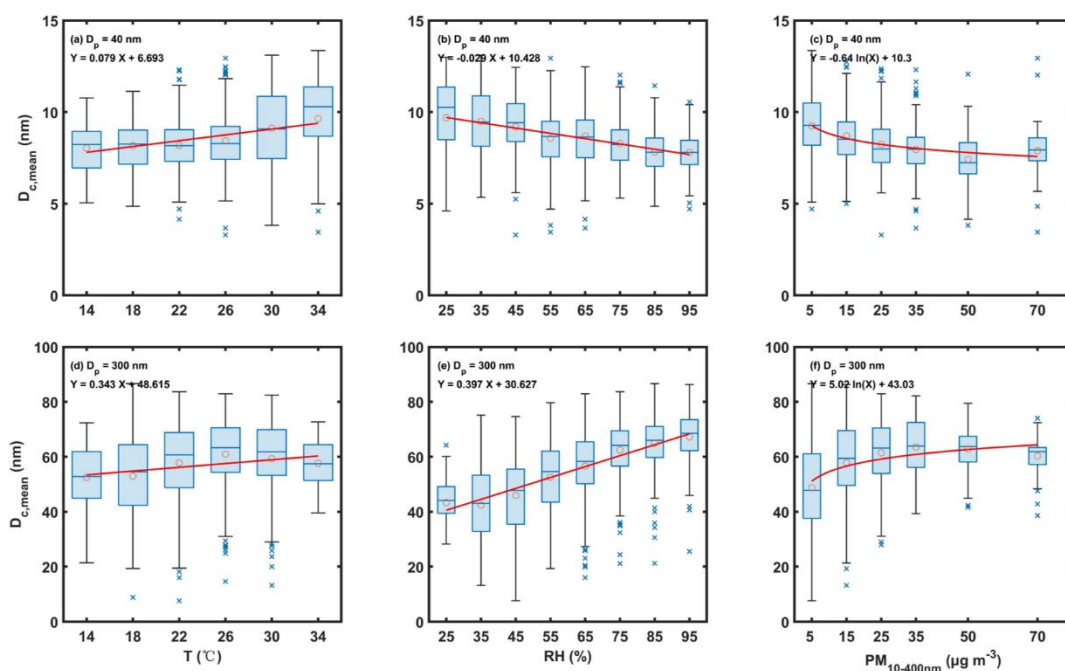
423 Figure 9 depicts a linear relationship between  $D_{c,\text{mean}}$  and RH, while a logarithmic relationship  
 424 between  $D_{c,\text{mean}}$  and  $\text{PM}_{10-400\text{nm}}$ .  $D_{c,\text{mean}}$  in the nucleation mode decreased with increasing RH and  
 425  $\text{PM}_{10-400\text{nm}}$  for nucleation-mode soot particles (Fig. 9b-c). This suggests that high ambient RH and  
 426 severe aerosol pollution events could inhibit the coating of nucleation-mode soot particles. Previous  
 427 studies have reported that aerosol pollution events were generally associated with high RH in the  
 428 NCP (G. Wang et al., 2016; Z. Wu et al., 2018). This suggests that highly polluted environments  
 429 with high ambient RH are not beneficial to the formation of new particles, leading to the weak  
 430 coating on nucleation-mode soot particles. However,  $D_{c,\text{mean}}$  in the accumulation mode increased  
 431 with increasing RH and  $\text{PM}_{10-400\text{nm}}$  (Fig. 9e-f). This suggests that highly polluted environments with  
 432 high ambient RH favor the growth of accumulation-mode soot particles by coating. This is possibly  
 433 related to enhanced liquid-phase chemical reactions under these environmental conditions.  
 434 Considering that accumulation-mode particles are the dominant components of  $\text{PM}_{10-400\text{nm}}$ , this  
 435 further implies that the coating on soot particles is important to the formation of heavy aerosol



436 pollution events. Y. Wang et al. (2019) indicated that the properties of ultrafine- and accumulation-  
 437 mode particles were distinct in clean and polluted urban environments due to the different particle  
 438 formation and growth processes. This study further indicates that it is also distinct in the aging of  
 439 soot particles.

440 In summary, high ambient  $T$  and RH levels appeared to promote the coating growth of  
 441 accumulation-mode soot particles in highly polluted environments. High ambient  $T$  but low RH  
 442 were beneficial to the coating growth of nucleation-mode soot particles in less polluted  
 443 environments.

444



445

446 **Figure 10.** Relationships between ensemble mean coating depth ( $D_{c,mean}$ ) and ambient  $T$  (a, d) and  
 447 RH (b, e), and  $PM_{10-400nm}$  (c, f) for 40-nm (top panels) and 300-nm (bottom panels) particles. The  
 448 circles show the mean  $D_{c,mean}$  with boxes showing the 25th, 50th, and 75th percentiles and  
 449 extremities show the 5th and 95th percentiles. Red lines show the linear or logarithmic fitting lines  
 450 through the data, and best-fit relations are given in each panel.

451

#### 452 4. Summary and conclusions

453 Soot particles containing most of the black carbon (BC) in the atmosphere are the most  
 454 important light-absorbing carbonaceous particles. Investigating the mixing state of soot particles in  
 455 the field is crucial to accurately model aerosol absorption and reduce the uncertainty of radiative  
 456 forcing caused by aerosols in climate models.

457 Here, over five months of volatility tandem differential mobility analyzer (VTDMA) data

458 collected at a heavily polluted suburban site (Xingtai, or XT) from May to October of 2016 were  
459 used to study the volatility and mixing state of size-resolved soot particles and their influencing  
460 factors. Ambient meteorological variables [temperature ( $T$ ), relative humidity (RH), and winds]  
461 varied between the warm (June, July, and August) and cold (May, September, and October) months  
462 of the field campaign. Variations in meteorological parameters could induce various aerosol aging  
463 processes and different levels of aerosol pollution, largely impacting the volatility and mixing state  
464 of soot particles.

465 The retrieved probability density function of the shrink factor ( $SF$ -PDF) at XT had three modes,  
466 demonstrating that the volatility and mixing state of soot-containing particles were more complex  
467 at XT than at other sites in the North China Plain. Compared with accumulation-mode soot particles,  
468 nucleation-mode soot-containing particles were more volatile and had a higher degree of internal  
469 mixing. The diurnal variation patterns of  $SF$ -PDFs suggest that coating by newly formed materials  
470 was the possible reason for the enhanced volatility of nucleation-mode soot-containing particles in  
471 the daytime. Moreover, the enhanced nocturnal secondary aerosol formation was responsible for the  
472 enhanced volatility of accumulation-mode soot-containing particles in the nighttime. The ensemble  
473 mean  $SF$  ( $SF_{\text{mean}}$ ) was size dependent and varied monthly. The monthly variations in  $SF_{\text{mean}}$  became  
474 larger with increasing particle size, implying a stronger seasonal variation of the coating effect on  
475 soot particles for larger-sized particles.

476 The similar diurnal variation trends of the number fraction of nonvolatile mode particles ( $NF_{\text{NV}}$ )  
477 in  $SF$ -PDFs and the mass concentration of BC ( $M_{\text{BC}}$ ) suggest that human activities had a negative  
478 influence on the volatility and degree of internal mixing of soot particles, especially for  
479 accumulation-mode soot-containing particles. In general, less externally mixed soot particles (i.e.,  
480 a smaller  $NF_{\text{NV}}$ ) were present in warm months than in cold months.  $NF_{\text{NV}}$  was always lower in the  
481 daytime than at night, suggesting a lower fraction of externally mixed soot particles in the daytime.  
482 This suggests that daytime photochemical reactions may promote the transformation of externally  
483 mixed soot particles into internally mixed soot particles. Moreover,  $NF_{\text{NV}}$  increased with increasing  
484 particle size, meaning a higher degree of external mixing for larger-sized particles. This also  
485 suggests that the degree of external mixing was higher for accumulation-mode soot particles than  
486 for nucleation-mode soot particles.

487 To explore factors influencing soot-particle volatility and mixing state, the ensemble mean  
488 coating depth ( $D_{\text{c,mean}}$ ) of volatile matter on soot particles was investigated.  $D_{\text{c,mean}}$  was thicker in  
489 warm months than in cold months, even though aerosol pollution was heavier in cold months. In  
490 warm months,  $D_{\text{c,mean}}$  was larger in July than in other months, likely because high  $T$ , high RH, and  
491 the stable atmospheric environment in July were conducive to the coating effect on soot particles.  
492 The relationships between  $D_{\text{c,mean}}$  and possible influencing factors (i.e.,  $T$ , RH, and  $\text{PM}_{10-400\text{nm}}$ ) show

493 that high ambient  $T$  and RH in a polluted environment promoted the coating growth of  
494 accumulation-mode soot particles. High ambient  $T$  but low RH in a clean environment was  
495 beneficial to the coating growth of nucleation-mode soot particles.

496 These results demonstrate great differences in the volatility and mixing state between nucleation-  
497 and accumulation-mode soot particles. The impact of anthropogenic emissions on the volatility and  
498 mixing state of soot-containing particles was clearly seen, especially for accumulation-mode soot-  
499 containing particles. The monthly variations in meteorological conditions and aerosol pollution  
500 levels may induce different aerosol aging processes, strongly impacting the volatility and mixing  
501 state of soot-containing particles. This study suggests that differences between the mixing states of  
502 nucleation- and accumulation-mode soot particles and their influencing factors should be considered  
503 in climate models.

504

505 *Acknowledgement.* This work was funded by the National Natural Science Foundation of China  
506 (NSFC) research project (grant no. 42030606, 42005067, 92044303), the National Key R&D  
507 Program of the Ministry of Science and Technology, China (grant no. 2017YFC1501702), and the  
508 Open Fund of State Key Laboratory of Remote Sensing Science (grant no. 202015). We also thank  
509 all participants in the campaign for their tireless work and cooperation.

510

511 *Data availability.* The measurement data from the field experiment used in this study are available  
512 from the first author upon request (yuyingwang@nuist.edu.cn).

513

514 *Author contributions.* YW conceived the study and led the overall scientific questions. YW,  
515 RH, and QW processed the measurement data and prepared this paper. ZL, MC copyedited the  
516 article. Other co-authors participated in the implementation of this experiment and the discussion  
517 of this paper.

518

519 *Competing interests.* The authors declare that they have no conflict of interest.

520

521

522

## 523 **References**

524 Adachi, K., Sedlacek, A. J., Kleinman, L., Chand, D., Hubbe, J. M., and Buseck, P. R.: Volume changes  
525 upon heating of aerosol particles from biomass burning using transmission electron microscopy,

526 Aerosol Sci. Tech., 52, 46-56, <https://doi.org/10.1080/02786826.2017.1373181>, 2018.

527 Adachi, K., Sedlacek, A. J., Kleinman, L., Springston, S. R., Wang, J., Chand, D., Hubbe, J. M., Shilling,  
528 J. E., Onasch, T. B., Kinase, T., Sakata, K., Takahashi, Y., and Buseck, P. R.: Spherical tarball  
529 particles form through rapid chemical and physical changes of organic matter in biomass-burning  
530 smoke, *Proceedings of the National Academy of Sciences*, 116, 19336-19341,  
531 <https://doi.org/10.1073/pnas.1900129116>, 2019.

532 Bellouin, N., Quaas, J., Gryspeerdt, E., Kinne, S., Stier, P., Watson-Parris, D., Boucher, O., Carslaw, K.  
533 S., Christensen, M., Daniau, A. L., Dufresne, J. L., Feingold, G., Fiedler, S., Forster, P., Gettelman,  
534 A., Haywood, J. M., Lohmann, U., Malavelle, F., Mauritsen, T., McCoy, D. T., Myhre, G.,  
535 Mülmenstädt, J., Neubauer, D., Possner, A., Rugenstein, M., Sato, Y., Schulz, M., Schwartz, S. E.,  
536 Sourdeval, O., Storelvmo, T., Toll, V., Winker, D., and Stevens, B.: Bounding global aerosol radiative  
537 forcing of climate change, *Rev. Geophys.*, 58, e2019R-e2660R, 2020.

538 Bond, T. C., Doherty, S. J., Fahey, D. W., Forster, P. M., Berntsen, T., DeAngelo, B. J., Flanner, M. G.,  
539 Ghan, S., Kärcher, B., Koch, D., Kinne, S., Kondo, Y., Quinn, P. K., Sarofim, M. C., Schultz, M. G.,  
540 Schulz, M., Venkataraman, C., Zhang, H., Zhang, S., Bellouin, N., Guttikunda, S. K., Hopke, P. K.,  
541 Jacobson, M. Z., Kaiser, J. W., Klimont, Z., Lohmann, U., Schwarz, J. P., Shindell, D., Storelvmo, T.,  
542 Warren, S. G., and Zender, C. S.: Bounding the role of black carbon in the climate system: A scientific  
543 assessment, *J. Geophys. Res. Atmos.*, 118, 5380-5552, <https://doi.org/10.1002/jgrd.50171>, 2013.

544 Cheng, Y. F., Berghof, M., Garland, R. M., Wiedensohler, A., Wehner, B., Müller, T., Su, H., Zhang, Y.  
545 H., Achtert, P., Nowak, A., Pöschl, U., Zhu, T., Hu, M., and Zeng, L. M.: Influence of soot mixing  
546 state on aerosol light absorption and single scattering albedo during air mass aging at a polluted  
547 regional site in northeastern China, *J. Geophys. Res. Atmos.*, 114, 2009.

548 Cheng, Y. F., Su, H., Rose, D., Gunthe, S. S., Berghof, M., Wehner, B., Achtert, P., Nowak, A.,  
549 Takegawa, N., Kondo, Y., Shiraiwa, M., Gong, Y. G., Shao, M., Hu, M., Zhu, T., Zhang, Y. H.,  
550 Carmichael, G. R., Wiedensohler, A., Andreae, M. O., and Pöschl, U.: Size-resolved measurement of  
551 the mixing state of soot in the megacity Beijing, China: diurnal cycle, aging and parameterization,  
552 *Atmos. Chem. Phys.*, 12, 4477-4491, 2012.

553 Cheung, H. H., Tan, H., Xu, H., Li, F., Wu, C., Yu, J. Z., and Chan, C. K.: Measurements of non-volatile  
554 aerosols with a VTDMA and their correlations with carbonaceous aerosols in Guangzhou, China,  
555 *Atmos. Chem. Phys.*, 16, 8431-8446, 2016.

556 Christensen, M., Gettelman, A., Cermak, J., Dagan, G., Diamond, M., Douglas, A., Feingold, G.,  
557 Glassmeier, F., Goren, T., Grosvenor, D., Gryspeerdt, E., Kahn, R., Li, Z., Ma, P. L., Malavelle, F.,  
558 McCoy, I., McCoy, D., McFarquhar, G., Mülmenstädt, J., Pal, S., Possner, A., Povey, A., Quaas, J.,  
559 Rosenfeld, D., Schmidt, A., Schrödner, R., Sorooshian, A., Stier, P., Toll, V., Watson-Parris, D.,  
560 Wood, R., Yang, M., and Yuan, T.: Opportunistic experiments to constrain aerosol effective radiative  
561 forcing, *Atmos. Chem. Phys. Discuss.*, 2021, 1-60, 2021.

562 Gustafsson, Ö., and Ramanathan, V.: Convergence on climate warming by black carbon aerosols, *Proc.*  
563 *Natl. Acad. Sci. U.S.A.*, 113, 4243, <https://doi.org/10.1073/pnas.1603570113>, 2016.

564 Hong, J., Äijälä, M., Häme, S. A. K., Hao, L., Duplissy, J., Heikkinen, L. M., Nie, W., Mikkilä, J.,  
565 Kulmala, M., Prisle, N. L., Virtanen, A., Ehn, M., Paasonen, P., Worsnop, D. R., Riipinen, I., Petäjä,  
566 T., and Kerminen, V. M.: Estimates of the organic aerosol volatility in a boreal forest using two  
567 independent methods, *Atmos. Chem. Phys.*, 17, 4387-4399, [https://doi.org/10.5194/acp-17-4387-](https://doi.org/10.5194/acp-17-4387-2017)  
568 2017, 2017.

569 Hossain, A. M. M. M., Park, S., Kim, J. S., and Park, K.: Volatility and mixing states of ultrafine particles

570 from biomass burning, *J. Hazard. Mater.*, 205-206, 189-197, 2012.

571 IPCC: Climate change 2021: The Physical Science Basis, sixth assessment of the Inter-governmental  
572 Panel on Climate Change, in press, 2021.

573 Kuniyal, J. C., and Guleria, R. P.: The current state of aerosol-radiation interactions: a mini review, *J.*  
574 *Aerosol Sci.*, 130, 45-54, 2019.

575 Levy, M. E., Zhang, R., Khalizov, A. F., Zheng, J., Collins, D. R., Glen, C. R., Yuan, W., Yu, X. Y.,  
576 Winston, L., and Jayne, J. T.: Measurements of submicron aerosols in Houston, Texas during the 2009  
577 SHARP field campaign, *J. Geophys. Res. Atmos.*, 118, 10,518-10,534,  
578 <https://doi.org/10.1002/jgrd.50785>, 2013.

579 Levy, M. E., Zhang, R., Zheng, J., Tan, H., Wang, Y., Molina, L. T., Takahama, S., Russell, L. M., and  
580 Li, G.: Measurements of submicron aerosols at the California - Mexico border during the Cal-Mex  
581 2010 field campaign, *Atmos. Environ.*, 88, 308-319, 2014. Li, Z., Wang, Y., Guo, J., Zhao, C., Cribb,  
582 M. C., Dong, X., Fan, J., Gong, D., Huang, J., Jiang, M., Jiang, Y., Lee, S. S., Li, H., Li, J., Liu, J.,  
583 Qian, Y., Rosenfeld, D., Shan, S., Sun, Y., Wang, H., Xin, J., Yan, X., Yang, X., Yang, X., Zhang, F.,  
584 and Zheng, Y.: East Asian Study of Tropospheric Aerosols and their Impact on Regional Clouds,  
585 Precipitation, and Climate (EAST-AIR<sub>CPC</sub>), *J. Geophys. Res. Atmos.*, 124, 13,026-13,054,  
586 <https://doi.org/10.1029/2019JD030758>, 2019.

587 Drinovec, L., Močnik, G., Zotter, P., Prévôt, A. S. H., Ruckstuhl, C., Coz, E., Rupakheti, M., Sciare, J.,  
588 Müller, T., Wiedensohler, A., and Hansen, A. D. A.: The "dual-spot" Aethalometer: an improved  
589 measurement of aerosol black carbon with real-time loading compensation, *Atmos. Meas. Tech.*, 8,  
590 1965-1979, <https://doi.org/10.5194/amt-8-1965-2015>, 2015.

591 Novakov, T., Ramanathan, V., Hansen, J. E., Kirchstetter, T. W., Sato, M., Sinton, J. E., and Sathaye, J.  
592 A.: Large historical changes of fossil-fuel black carbon aerosols, *Geophys. Res. Lett.*, 30,  
593 <https://doi.org/10.1029/2002GL016345>, 2003.

594 Peng, J., Hu, M., Guo, S., Du, Z., Zheng, J., Shang, D., Zamora, M. L., Zeng, L., Shao, M., and Wu, Y.:  
595 Markedly enhanced absorption and direct radiative forcing of black carbon under polluted urban  
596 environments, *Proc. Natl. Acad. Sci. U.S.A.*, 113, 4266-4271, 2016.

597 Peng, J., Hu, M., Shang, D., Wu, Z., Du, Z., Tan, T., Wang, Y., Zhang, F., and Zhang, R.: Explosive  
598 secondary aerosol formation during severe haze in the North China Plain, *Environ. Sci. Technol.*, 55,  
599 2189-2207, <https://doi.org/10.1021/acs.est.0c07204>, 2021.

600 Philippin, S., Wiedensohler, A., and Stratmann, F.: Measurements of non-volatile fractions of pollution  
601 aerosols with an eight-tube volatility tandem differential mobility analyzer (VTDMA-8), *J. Aerosol*  
602 *Sci.*, 35, 185-203, <https://doi.org/10.1016/j.jaerosci.2003.07.004>, 2004.

603 Ramana, M. V., Ramanathan, V., Feng, Y., Yoon, S., Kim, S., Carmichael, G. R., and Schauer, J. J.:  
604 Warming influenced by the ratio of black carbon to sulphate and the black-carbon source, *Nat. Geosci.*,  
605 3, 542-545, <https://doi.org/10.1038/ngeo918>, 2010.

606 Ren, R., Li, Z., Yan, P., Wang, Y., Wu, H., Cribb, M., Wang, W., Jin, X., Li, Y., and Zhang, D.:  
607 Measurement report: the effect of aerosol chemical composition on light scattering due to the  
608 hygroscopic swelling effect, *Atmos. Chem. Phys.*, 21, 9977-9994, 2021.

609 Seinfeld, J. H., Bretherton, C., Carslaw, K. S., Coe, H., DeMott, P. J., Dunlea, E. J., Feingold, G., Ghan,  
610 S., Guenther, A. B., Kahn, R., Kraucunas, I., Kreidenweis, S. M., Molina, M. J., Nenes, A., Penner, J.  
611 E., Prather, K. A., Ramanathan, V., Ramaswamy, V., Rasch, P. J., Ravishankara, A. R., Rosenfeld,  
612 D., Stephens, G., and Wood, R.: Improving our fundamental understanding of the role of aerosol-

613 cloud interactions in the climate system, *Proc. Natl. Acad. Sci. U.S.A.*, 113, 5781, 2016.

614 Stolzenburg, M. R., and McMurry, P. H.: TDMAFIT user's manual, University of Minnesota,  
615 Department of Mechanical Engineering, Particle Technology Laboratory, Minneapolis, 1-61, 1988.

616 Stolzenburg, M. R., and McMurry, P. H.: Equations governing single and tandem DMA configurations  
617 and a new lognormal approximation to the transfer function, *Aerosol Sci. Tech.*, 42, 421-432, 2008.

618 Swietlicki, E., Hansson, H. C., Hämeri, K., Svenningsson, B., Massling, A., Mcfiggans, G., McMurry, P.  
619 H., Petäjä, T., Tunved, P., Gysel, M., Topping, D., Weingartner, E., Baltensperger, U., Rissler, J.,  
620 Wiedensohler, A., and Kulmala, M.: Hygroscopic properties of submicrometer atmospheric aerosol  
621 particles measured with H-TDMA instruments in various environments—a review, *Tellus B: Chem.*  
622 *Phys. Meteor.*, 60, 432-469, <https://doi.org/10.1111/j.1600-0889.2008.00350.x>, 2008.

623 Twohy, C. H., Coakley Jr., J. A., and Tahnk, W. R.: Effect of changes in relative humidity on aerosol  
624 scattering near clouds, *J. Geophys. Res. Atmos.*, 114, 2009.

625 Wang, G., Zhang, R., Gomez, M. E., Yang, L., Zamora, M. L., Hu, M., Lin, Y., Peng, J., Guo, S., and  
626 Meng, J.: Persistent sulfate formation from London Fog to Chinese haze, *Proc. Natl. Acad. Sci. U.S.A.*,  
627 113, 13,630-13,635, 2016.

628 Wang, J., Liu, D., Ge, X., Wu, Y., Shen, F., Chen, M., Zhao, J., Xie, C., Wang, Q., Xu, W., Zhang, J.,  
629 Hu, J., Allan, J., Joshi, R., Fu, P., Coe, H., and Sun, Y.: Characterization of black carbon-containing  
630 fine particles in Beijing during wintertime, *Atmos. Chem. Phys.*, 19, 447-458,  
631 <https://doi.org/10.5194/acp-19-447-2019>, 2019.

632 Wang, Y., Zhang, F., Li, Z., Tan, H., Xu, H., Ren, J., Zhao, J., Du, W., and Sun, Y.: Enhanced  
633 hydrophobicity and volatility of submicron aerosols under severe emission control conditions in  
634 Beijing, *Atmos. Chem. Phys.*, 17, 5239-5251, <https://doi.org/10.5194/acp-17-5239-2017>, 2017.

635 Wang, Y., Li, Z., Zhang, Y., Du, W., Zhang, F., Tan, H., Xu, H., Fan, T., Jin, X., Fan, X., Dong, Z.,  
636 Wang, Q., and Sun, Y.: Characterization of aerosol hygroscopicity, mixing state, and CCN activity at  
637 a suburban site in the central North China Plain, *Atmos. Chem. Phys.*, 18, 11,739-11,752,  
638 <https://doi.org/10.5194/acp-18-11739-2018>, 2018.

639 Wang, Y., Li, Z., Zhang, R., Jin, X., Xu, W., Fan, X., Wu, H., Zhang, F., Sun, Y., Wang, Q., Cribb, M.,  
640 and Hu, D.: Distinct ultrafine- and accumulation-mode particle properties in clean and polluted urban  
641 environments, *Geophys. Res. Lett.*, 46, 10,918-10,925, <https://doi.org/10.1029/2019GL084047>, 2019.

642 Wang, Y., Wang, J., Li, Z., Jin, X., Sun, Y., Cribb, M., Ren, R., Lv, M., Wang, Q., Gao, Y., Hu, R.,  
643 Shang, Y., and Gong, W.: Contrasting aerosol growth potential in the northern and central-southern  
644 regions of the North China Plain: implications for combating regional pollution, *Atmos. Environ.*,  
645 267, 118723, <https://doi.org/10.1016/j.atmosenv.2021.118723>, 2021.

646 Wehner, B., Berghof, M., Cheng, Y. F., Achtert, P., Birmili, W., Nowak, A., Wiedensohler, A., Garland,  
647 R. M., Pöschl, U., and Hu, M.: Mixing state of nonvolatile aerosol particle fractions and comparison  
648 with light absorption in the polluted Beijing region, *J. Geophys. Res. Atmos.*, 114, 85-86, 2009.

649 Wu, Y., Wang, X., Tao, J., Huang, R., Tian, P., Cao, J., Zhang, L., Ho, K. F., Han, Z., and Zhang, R.:  
650 Size distribution and source of black carbon aerosol in urban Beijing during winter haze episodes,  
651 *Atmos. Chem. Phys.*, 17, 7965-7975, <https://doi.org/10.5194/acp-17-7965-2017>, 2017.

652 Wu, Z., Wang, Y., Tan, T., Zhu, Y., Li, M., Shang, D., Wang, H., Lu, K., Guo, S., Zeng, L., and Zhang,  
653 Y.: Aerosol liquid water driven by anthropogenic inorganic salts: implying its key role in haze  
654 formation over the North China Plain, *Environ. Sci. Tech. Lett.*, 5, 160-166,  
655 <https://doi.org/10.1021/acs.estlett.8b00021>, 2018.

656 Zhang, F., Wang, Y., Peng, J., Chen, L., Sun, Y., Duan, L., Ge, X., Li, Y., Zhao, J., Liu, C., Zhang, X.,

657 Zhang, G., Pan, Y., Wang, Y., Zhang, A. L., Ji, Y., Wang, G., Hu, M., Molina, M. J., and Zhang, R.:  
658 An unexpected catalyst dominates formation and radiative forcing of regional haze, *Proc. Natl. Acad.*  
659 *Sci. U.S.A.*, 117, 3960, <https://doi.org/10.1073/pnas.1919343117>, 2020.

660 Yu, C., Liu, D., Broda, K., Joshi, R., Olfert, J., Sun, Y., Fu, P., Coe, H., and Allan, J. D.: Characterising  
661 mass-resolved mixing state of black carbon in Beijing using a morphology-independent measurement  
662 method, *Atmos. Chem. Phys.*, 20, 3645-3661, <https://doi.org/10.5194/acp-20-3645-2020>, 2020.

663 Zhang, S. L., Ma, N., Kecorius, S., Wang, P. C., Hu, M., Wang, Z. B., Größ, J., Wu, Z. J., and  
664 Wiedensohler, A.: Mixing state of atmospheric particles over the North China Plain, *Atmos. Environ.*,  
665 125, Part A, 152-164, <https://doi.org/10.1016/j.atmosenv.2015.10.053>, 2016.

666 Zhang, Y., Zhang, Q., Cheng, Y., Su, H., Kecorius, S., Wang, Z., Wu, Z., Hu, M., Zhu, T., Wiedensohler,  
667 A., and He, K.: Measuring the morphology and density of internally mixed black carbon with SP2  
668 and VTDMA: new insight into the absorption enhancement of black carbon in the atmosphere, *Atmos.*  
669 *Meas. Tech.*, 9, 1833-1843, <https://doi.org/10.5194/amt-9-1833-2016>, 2016.

670 Zhang, Y., Du, W., Wang, Y., Wang, Q., Wang, H., Zheng, H., Zhang, F., Shi, H., Bian, Y., Han, Y., Fu,  
671 P., Canonaco, F., Prévôt, A. S. H., Zhu, T., Wang, P., Li, Z., and Sun, Y.: Aerosol chemistry and  
672 particle growth events at an urban downwind site in North China Plain, *Atmos. Chem. Phys.*, 18,  
673 14,637-14,651, <https://doi.org/10.5194/acp-18-14637-2018>, 2018.

674 Zhang, Y., Liu, H., Lei, S., Xu, W., Tian, Y., Yao, W., Liu, X., Liao, Q., Li, J., Chen, C., Sun, Y., Fu, P.,  
675 Xin, J., Cao, J., Pan, X., and Wang, Z.: Mixing state of refractory black carbon in fog and haze at  
676 rural sites in winter on the North China Plain, *Atmos. Chem. Phys.*, 21, 17631-17648,  
677 <https://doi.org/10.5194/acp-21-17631-2021>, 2021.

678 Zhou, C., Zhang, H., Zhao, S., and Li, J.: Simulated effects of internal mixing of anthropogenic aerosols  
679 on the aerosol-radiation interaction and global temperature, *Int. J. Climatol.*, 37, 972-986, 2017.

680